Effect of Different Inlet/Outlet Port Configurations on the Thermal Management of Prismatic Li-ion Batteries

Gurjeet Singh[1], and Hongwei Wu[2]

[1]Department of Mechanical Engineering, Yeshwantrao Chavan College of Engineering (YCCE), Nagpur, Maharashtra-441110, India

[2]School of Physics, Engineering and Computer Science, University of Hertfordshire, Hatfield, AL10 9AB, United Kingdom

[1]Corresponding author

Email: gurjeetpunia4@gmail.com

Abstract

The performance and life cycle of Li-ion batteries are governed by the maximum temperature and uniformity of temperature distribution in the battery pack and an efficient thermal management system is highly desired to keep the operating temperature of battery pack within safe operating limits. Air-cooling has received an extensive attention in the area of battery thermal management however, performance intensification of air-cooling modules is quite essential while keeping the simplicity of design to satisfy the weight and space constraints of the electric vehicle applications. Therefore, in the current work, efforts have been made to design a simple and generalized air-cooling module for the efficient thermal management of the Li-ion batteries. The current work explored the effect of two common air flow configurations: side inlet and side outlet (SS) and side inlet and front outlet (SF), with different number of inlet/ outlet ports (single inlet and single outlet, single inlet and two outlets, two inlets and single outlet, and two inlets and two outlets) on the thermal and hydraulic performance of the Li-ion battery pack. Subsequently, a new design of battery module with an open outlet port is proposed. It is observed that the way fluid leaves the cooling module significantly influences the flow and temperature distribution uniformity of the battery pack. Significant improvement in the fluid flow distribution and lower temperature fluctuation are maintained by the SF designs as compared to the SS designs. Among all SS designs, only SS-Ib at $V_{in} \geq 5.6$ m/s and SS-IV at $V_{in} \geq 4.8$ m/s are found suitable for the thermal management of Li-ion battery pack, whereas all SF designs maintained desired T_{max} and ΔT_{max} conditions at $V_{in} \geq 4.8$ m/s. Furthermore, the new design (SF-V) with an open outlet results in the reduction of T_{max} by 7 °C and ΔT_{max} by 64.5% as compared to base design (SS-Ia) at same pressure drop penalty.

Keywords: *Electric vehicles; Lithium-ion battery; heat generation; flow non-uniformity; temperature fluctuation; air-cooling*

1. INTRODUCTION

Environment degradation by the rapid surge in the global carbon emissions during the past century has become a threat to the sustainable development all over the world. Utilization of natural energy resources, primarily fossil fuels (e.g. oil, gas, and coal), is the main contributor in the emission of greenhouse gases (GHG), which are responsible for global warming. Although the Paris Climate Conference led to a new climate legal agreement for all countries to curb the global warming at 1.5 °C – 2 °C [1], detrimental consequences of climate change cannot be avoided. Therefore, fulfilling current energy requirements in a sustainable manner is an ongoing challenge. It is observed that the worldwide consumption of oil is increased by 1.9 million barrels per day and 66% of which is consumed alone by the transport sector [2]. The research area in the development and utilization of green energy and clean vehicles has received pre-eminent attention to curb the emissions of GHSs and avoid energy crisis. Clean vehicles, including pure electric vehicles (EVs), hybrid electric vehicles (HEVs), plug-in hybrid electric vehicles and fuel cell electric vehicles, compared to conventional internal combustion vehicles, are effective to reduce GHSs and pollutants emission [3-7]. It is estimated that using renewable electric power resources and EVs could reduce the GHS emissions up to 40% [8]. Furthermore, with the rising interest and focus on the EVs, it is expected the 35% of the new cars will be electrified by 2040 [9].

Battery module acts as a source of energy for the clean vehicles, and in this regard, Lithium-ion (Li-ion) based batteries are proven to be more advantageous as compared to lead acid batteries due to their high energy density, low self-discharge rate, good stability, and high voltage. However, due to the electrochemical reaction inside the battery cell, the generated heat would affect the temperature distribution in the battery cells. The permissible temperature range during the discharging operation of Li-ion battery is −20 to 60 °C, whereas for the optimal performance,

temperature range of 20 to 40 °C must be maintained [10]. Furthermore, maintaining uniformity of temperature distribution among different cells is another important aspect, and high temperature difference among different battery cells may lead to different state of charge. Consequently, it results in electrical imbalance and performance degradation of the battery module. A maximum temperature difference lower than 5 °C has to be maintained for the efficient performance of the battery pack. The necessity to curb the maximum temperature rise and keep the temperature difference among battery cells below a certain limit, an efficient thermal management is required during normal as well as worse working conditions.

Various thermal management techniques, such as air-cooling [10], liquid cooling [11-16], heat pipes [17-20] and phase change materials (PCMs) [21-25], have been studied in the last decade to dissipate the heat generation from the Li-ion battery packs. It is found that the liquid cooling techniques are very effective to restrict the maximum temperature rise (T_{max}) and temperature difference among battery cells (ΔT_{max}) in the desirable range; however, it increases the complexity, weight, and cost of the cooling system. Furthermore, the liquid cooling using water is associated with the risk of short-circuits, and the use of hydrocarbons, such as silicon oil, is associated with high pressure drop. Use of PCMs has also received a significant attention due to the simple design; nevertheless, their capacity of dissipating heat is limited and is only applicable for low discharge rates [26]. Additionally, PCM cooling systems require external air-cooling to dissipate the absorbed heat by PCM to the atmosphere. Thermal management of Li-ion batteries using air-cooling has been widely explored due to their simple construction, light weight, less pumping power requirement, less price and easy maintenance. In addition, space constraints in some applications, such as two wheelers, restricts the deployment of liquid cooling or PCM based cooling modules; therefore, in such applications, air cooling modules are expected to maintain the

desired thermal-hydrodynamic environment. As a result, a lot of attention has been focused on the air-cooling modules in the last decade for its application in the cooling of Li-ion battery packs.

Mahamud and Park [27] numerically studied the cooling of cylindrical Li-ion cells using reciprocating air flow technique. It was noticed that for the reciprocating air flow arrangement the T_{max} and ΔT_{max} are reduced by 4 °C and 1.5 °C, respectively as compared to the case of unidirectional air flow. They attributed it to the redistribution of heat and interruption of the boundary layers due to the periodic reciprocating flow. Na et al. [28] studied the two air flow arrangements: unidirectional air flow and reverse layered air flow, to cool the Li-ion battery cells of cylindrical shape. They observed that reversed flow arrangement helps to reduce the T_{max} and ΔT_{max} by 0.6 °C and 1.1 °C, respectively, as compared to the unidirectional air flow. Furthermore, an experimental setup is fabricated to validate the simulation results. The battery cells in the experimental work are replicated by 20 heating rods, and heat generation from heating rods is maintained for battery at a discharge rate of 3C by supplying AC voltage to the heating rods. A good agreement is observed with the experimental results and numerical findings. Shahid and Agelin-Chaab [29] used a passive approach of secondary inlet plenum to achieve temperature uniformity in the 32 cylindrical cells of Li-ion battery pack. It is observed that the T_{max} and ΔT_{max} are improved by 9% and 39%, respectively, for the best case as compared to the base case. It is accredited to the enhanced mixing and turbulence in the air flow by addition of secondary plenum. E et al. [30] compared the thermal performance of Li-ion battery module with natural convection and forced air-convection with different air inlet and outlet flow location strategies and addition of baffles. They noticed better temperature distribution and lower T_{max} for air inlet and outlet location on different sides as compared to the inlet and outlet location on the same wall. Furthermore, addition of waffles results in the uniformity of air flow near the inlet and leads to

significant reduction in the temperature of the battery module. Three different configurations (aligned, staggered and cross) of 32 high energy density cylindrical Li-ion battery cells have been studied experimentally by Fan et al. [10]. It is noticed that the aligned configuration provided best cooling, whereas the staggered and cross configuration offered worse thermal performance and high pressure drop penalty due to increased resistance to the air flow. Wang et al. [31] studied the cooling performance of air-cooling system for large-scale Li-ion battery with 30 cylindrical 18650 type cells. The battery is charged at 1C rate and discharge at three variable rates of 1C, 1.5C and 2C. Two configurations of outlet ports are considered as case 1 (opening at top perpendicular to the inlet port) and case 2 (opening on opposite side of the inlet port). It is observed that temperature difference is lower for case 1 as compared to case 2. The cooling efficiency is found to be 73% and 62.3% for case 1 and case 2, respectively.

Fan et al. [32] simulated 8 prismatic cells of Li-ion battery module in vertical orientation with equal spacing using air as a cooling media. They studied the effect of gap spacing between the cells and flow rate on the temperature distribution in the battery module. It is observed that the maximum rise in cell temperature reduces for lower gap and higher flow rate. Xie et al. [33] studied the effect of inlet plenum angle, outlet plenum angle and gap size between the batteries on the thermal performance of an air-cooled system for cylindrical Li-ion batteries. It is noticed that the best thermal performance is obtained for 2.5 ° angles for both inlet and outlet plenums, and equal width of channels. The T_{max} and ΔT_{max} are found to be reduced by 12.8% and 29.7%, respectively, with the optimized method. Hong et al. [34] carried out 2D numerical simulations to study the forced air-cooling of Li-ion battery cells of rectangular shape. The T_{max} and ΔT_{max} are found to be beyond the safe working operation of the Li-ion battery. They explored different positions of the secondary vents near the outlet and found that the location of secondary vent strongly influences

the temperature distribution of the battery module. Reduction in the T_{max} by 5 °C and ΔT_{max} by 60% is observed for the best modified design as compared to the conventional design. Chen et al. [35] optimized the battery cell spacing to achieve homogenization in air flow distribution. Flow resistance network model [36] was used to calculate the air flow in the cooling channels, and flow distribution among channels could be improved by adding a modification factor so that the flow area of channels can be increased/ decreased based on the existing low/ high flow rate. It is noticed that for the best optimized design, T_{max} is reduced by 4 °C, and temperature difference is reduced by 69% as compared to the conventional design. Furthermore, Chen et al. [37] studied the cooling performance of battery air cooling module by optimizing the plenum angles and width of inlet and outlet port for U-type flow configuration. It is observed that the thermal performance of the battery cooling system is significantly improved for the optimized width of inlet and outlet ports, whereas the plenum angles might not contribute to any performance improvement. Temperature difference and power consumption are reduced by 70% and 32%, respectively, for the best optimized design. Li et al. [38] carried out experimental and numerical observations to study the cooling potential of air on copper mesh coupled double silica cooling plate for pouch Li-ion batteries. The effect of silica cooling plate thickness (0.5 – 2.5 mm), single/ double silica cooling plates, air velocity, air inlet position and number of cooling fans have been investigated. It is noticed that the T_{max} and ΔT_{max} decrease with increase in the thickness of silica cooling plate, air inlet velocity and number of fans. They recommend 1.5 mm as the optimum thickness for the silica cooling plate. The fan's position offers better heat transfer when place at the front side as compared to the side position. Wang et al. [39] experimentally explored the effect of reciprocating air flow on the laminated Li-ion battery. An infrared imager is used to record the temperature distribution in the battery during charge and discharge process. To keep the ΔT_{max} below permissible limit of 5 °C, an aperiodic

reciprocating air flow control strategy is designed which reverses the air flow as the temperature difference approached to 4.9 °C. Furthermore, enhancement in thermal performance is achieved by increasing the air flow rate and with the usage of thinner air flow passage. Liu and Zhang [40] proposed a J-type flow configuration for the air-cooled thermal management of the Li-ion battery. The proposed configuration was made flexible by providing two ports at the outlet. The flow through both the outlets is controlled by two control valves. It is observed that J-type results in significant improvement of the temperature uniformity. Furthermore, a surrogate-based optimization is performed to improve the performance of U, Z and J-type configuration, and it is noticed that for the optimal case, the temperature rise is reduced by 35.3%, 46.6% and 31.18%, respectively, for three designs. Effect of battery pack shape on temperature distribution inside the battery was studied by Kang et al. [41]. Two shapes of battery packs: square and rectangular, are obtained by different arrangement of cylindrical Li-ion battery cells for the combined numerical and experimental analysis. It is observed that the inner temperature distribution at the center and side is different for both the packing. High temperature rise is noticed for the square battery pack at the center as compared to the rectangular pack. The later design offers higher convective heat exchange coefficient due to which its heat dissipation potential is high. Zhang et al. [42] studied the effect of provided flow restrictors (spoilers) in the inlet manifold of Li-ion battery packs with 8 prismatic cells. It is noticed that for the best number (5 spoilers) and position of spoilers (4^{th} to 8^{th} distributor section) the T_{max} and ΔT_{max} are reduced by 1.86 °C and 2.77 °C, respectively as compared to the base case (no spoilers). Furthermore, improvement in the thermal performance is also achieved by optimizing the height of spoilers and size of manifolds. Ma et al. [43] numerically studied the effect of installing silica cooling plates between the prismatic Li-ion battery cells and

tampering of inlet manifold on the performance air-cooled Li-ion battery pack. It is noticed that with addition of silica plates, the T_{max} and ΔT_{max} reduced by 10 °C and 2.5 °C, respectively.

Moreover, considering the various advantages of the air-cooling systems over the other cooling modules, it became very critical to design an efficient air-cooling module so that the desired thermal characteristics of the Li-ion battery modules can be maintained. It is noticed that past researchers have studied the effect of air flow direction, outlet vents, silica cooling plates and flow configurations on the thermal performance of Li-ion battery packs. Table 1 summaries the comparison of various studies on the air-cooling battery packs with cylindrical and prismatic / pouch cells. It is noticed that the methods of alternation in the air flow direction results in a complex design of cooling module due to the requirement of additional sensors and secondary blowers, whereas the method of installing silica cooling plates is expected to increase the overall weight and power consumption of the cooling pack. It is also observed that the desired conditions of T_{max} and ΔT_{max} for the optimum thermal performance of Li-ion battery pack are only maintained by Hong et al. [34] and Liu and Zhang [39]; however, the applicability of both proposed methods is limited to their specific manifold designs (side inlet and side outlet) only. Moreover, in the current work, efforts have been made to design a simple and generalized air-cooling module for the efficient thermal management of the Li-ion batteries. The current work investigated the effect of two common air flow configurations: side inlet and side outlet (SS) and side inlet and front outlet (SF), with different number of inlet/ outlet ports (single inlet and single outlet, single inlet and two outlets, two inlets and single outlet, and two inlets and two outlets) for the thermal management of Li-ion battery pack. Subsequently, a new design of battery pack with best thermal-hydrodynamic performance is proposed. Finally, the thermal performance of all the designs

(suitable for maintaining the desired T_{max} and ΔT_{max} conditions) is compared at same pressure drop penalty.

2. Geometric Description

In the current work, a Li-ion battery module consisting of 12 prismatic cells is considered. The dimensions of battery cells are: L_{cell} = 151 mm, W_{cell} = 16 mm and H_{cell} = 65 mm. The properties of the battery and air are given in Table 2 [34]. A 3D model of the battery pack for the base design is shown in Fig. 1. Air enters in the battery module from the lower end and leaves from the top end as shown in Fig. 1. The distance between battery cells and distance of cells from the wall of battery case is kept as 3 mm. Other dimensions of the inlet and outlet manifolds are also given in Fig. 1. In the present study, two different categories of inlet and outlet flow arrangements: (1) side inlet and side outlet (SS), and (2) side inlet and front outlet (SF) designs are studied as shown in Fig. 2. Furthermore, each category is divided based on the number of inlet and outlet ports. These cases can also be divided into single inlet and single outlet (SS-Ia, SS-Ib and SF-I), single inlet and two outlets (SS-II and SF-II), two inlets and single outlet (SS-III and SF-III), and two inlets and two outlets (SS-IV and SF-IV).

In the different SS cases (Fig. 2 (a)), designs SS-Ia and SS-IIb are considered to investigate the effect of the location of outlet port on the opposite and same walls, respectively and in design SS-II, the effect of outlet port location is eliminated by providing two ports. In designs SS-III and SS-IV, the effect of addition of two inlet ports with respect to the combination of single outlet and two outlet ports is studied, respectively. In the SF designs, similar effect of adding two outlet ports for single inlet and two inlet ports is studied in the SF-II and SF-IV designs, respectively and in designs SF-I and SF-III, effect of providing single and two inlet ports respectively is investigated for single

outlet case. Furthermore, a new design (SF-V) is proposed in which effect of outlet port is removed by providing an open front outlet.

3. NUMERICAL MODELLING

3.1 Governing equations

Heat transfer and fluid flow characteristics in current numerical model are captured by solving generalized mass, momentum and energy conservation equations. The following assumptions have been considered for the current mathematical modelling:

(i) The effects of body and surface tension forces are neglected.

(ii) Effect of radiation and natural convection heat transfer are neglected.

(iii) Air is assumed to be continuum and incompressible.

(iv) Flow is assumed to be turbulent based on the value of Re.

The air flow is assumed to be in turbulent flow regime based on the Re values as given in Table 3, and k-epsilon model is used for the solution of the governing equations. k-epsilon is selected due to its good accuracy, convergence, and low memory requirements. Similar numerical modelling is also adopted by Refs. [34,35]. Following are the governing equations for the steady air flow with above mentioned assumptions.

3.1.1 Fluid section

Mass conservation equation:

$$\frac{\partial u_i}{\partial x_i} = 0 \tag{1}$$

Momentum conservation equations:

$$\rho u_j \frac{\partial u_i}{\partial x_j} = -\frac{\partial P}{\partial x_i} + \frac{\partial}{\partial x_j}\left[(\mu + \mu_t)\frac{\partial u_i}{\partial x_i}\right] \tag{2}$$

$$\rho u_j \frac{\partial k}{\partial x_j} = \frac{\partial}{\partial x_j}\left[(\mu + \frac{\mu_t}{\sigma_k})\frac{\partial k}{\partial x_j}\right] + \frac{\mu_t}{2}\left[\frac{\partial u_i}{\partial x_j} + \frac{\partial u_j}{\partial x_i}\right]^2 - \rho\epsilon \quad (3)$$

$$\rho u_j \frac{\partial \epsilon}{\partial x_j} = \frac{\partial}{\partial x_j}\left[(\mu + \frac{\mu_t}{\sigma_\epsilon})\frac{\partial \epsilon}{\partial x_j}\right] + c_1 \frac{\mu_t}{2}\left[\frac{\partial u_i}{\partial x_j} + \frac{\partial u_j}{\partial x_i}\right]^2 \frac{\epsilon}{k} - c_2 \rho \frac{\epsilon^2}{k} \quad (4)$$

Energy conservation equation:

$$\rho c_p u_j \frac{\partial \mathrm{T}}{\partial x_j} = \frac{\partial}{\partial x_j}\left[(\lambda + \frac{\mu_t}{\sigma_T})\frac{\partial T}{\partial x_j}\right] \quad (5)$$

where, P, μ, λ, c_p are Reynolds-averaged pressure, dynamic viscosity component, thermal conductivity, and specific heat, respectively. u_i and u_j denote Reynolds-averaged velocity components. Turbulent dynamic viscosity component (μ_t) is calculated by Eq. (6).

$$\mu_t = \rho C_\mu \frac{k^2}{\epsilon} \quad (6)$$

where, C_μ = 0.09

The turbulent kinetic energy and dissipation rate of the turbulent kinetic energy are defined by k and ϵ, respectively. The typical values of the parameters C_1, C_2, σ_k, σ_ϵ, σ_T are shown below.

C_1 = 1.44; C_2 = 1.92; σ_k = 1.0; σ_ϵ = 1.3; σ_T = 0.85

3.1.2 Solid section

Energy conservation equation:

$$\frac{\partial}{\partial x_j}\left[\lambda_s \frac{\partial T_s}{\partial x_j}\right] + \phi_g = 0 \quad (7)$$

where, subscript s denotes solid section, and ϕ_g represents heat generation rate.

3.2 Boundary conditions

Constant air velocity and temperature are assumed at the inlet of the cooling module. Different air velocities are used in current work as given in Table 3. The air inlet temperature is kept fixed at 300 K. All the outer walls are assumed to be adiabatic. The interface of battery surface and fluid sections are coupled, and heat generated in the battery cells is carried away by the forced air flow from the battery-fluid interface. No slip boundary condition is assumed at the interface. At the outlet of the cooling module, atmospheric pressure boundary condition is assigned. Heat generation (ϕ_g) inside the battery cells is assumed at constant rate of 41408 W/m^3 [34].

3.3 Solution procedure

All governing equations are solved by adopted the given boundary conditions by using ANSYS FLUENT 16.0. All the partial differential equations are discretized by using a finite volume method (FVM). Second order upwind scheme is used for the discretization of the momentum and energy equations. Pressure values are obtained by adopting standard discretization scheme. Pressure-velocity coupling is obtained by using the semi-implicit method for pressure linked equations (SIMPLE) algorithm. Convergence criteria is considered as 10^{-6} for the residuals of mass, momentum and energy equations.

3.4 Grid Independence analysis and model validation

Prior to the numerical simulations, a grid independence study has been carried to make the numerical model independent of grid size. In the current study, a 2D numerical model is used for the numerical simulation based on the observation of Hong et al. [34]. Hong et al. [34] compared the numerical results for the 3D and 2D numerical models with similar dimension of battery pack, and it is observed that 2D model is sufficient for the accurate estimation of fluid flow and heat transfer characteristics. In the current work, 5 different grid schemes have been studied, and the results of maximum temperature and overall pressure drop are given in Table 4. Non-uniform

hexahedral grid elements are generated using ICEM with smallest grid element dimension as 0.1 mm near the walls. It is noticed that for grid elements of 26×10^5 and 32×10^5, absolute deviation (AD) between overall pressure drop and maximum temperature is less than 1%. Therefore, 26×10^5 grid elements are used to save the computational time.

Validation of current numerical model is also carried out by comparing the results of Nu with the correlation of Nacke et. al. [44] for the SS-Ia design. Results of Nu from current numerical study and Eq. (8) are compared in Fig. 3. Mean absolute deviation of 10.6 % is noticed in calculation of Nu with respect to the Eq (8), which proves the accuracy of current numerical results.

$$Nu = \left[\frac{RePr}{L/D_h}\right]^{1/3} \left(\frac{\mu_a}{\mu_{a,s}}\right)^{0.14} \tag{8}$$

4. RESULTS AND DISCUSSION

In the current design, air enters from the common inlet port and then distributes across all channels around the battery cells and leaves through the outlet port. To measure the unevenness of air flow distribution in the battery pack, a velocity non-uniformity factor (α) is calculated as given by Eq. (9). Similar method is also used by Refs. [45, 46] to estimate the flow maldistribution factor among the parallel channels.

$$\alpha = \frac{V_{max} - V_{min}}{V_{avg}} \times 10 \tag{9}$$

where, V_{max}, V_{min} and V_{avg} represent the maximum, minimum and average velocity of air in the channels.

$$V_{avg} = \frac{\sum_{ch=1}^{ch=13} V_{ch}}{13} \tag{10}$$

To design a cooling system for the Li-ion battery pack, two prerequisite conditions are set based on the magnitude of maximum temperature (T_{max}) and maximum temperature fluctuation ($\Delta T_{max} = T_{max} - T_{min}$) as given below:

1st condition: $T_{max} \leq 40$ °C

2nd condition: $\Delta T_{max} \leq 5$ °C

Therefore, a design which satisfies both the conditions is considered as suitable for the thermal management of Li-ion battery pack.

4.1 Air flow distribution

4.1.2 Comparison of fluid flow distribution for SS designs

Fig. 4 (a) and (b) compares the air velocity distribution in different channels and velocity non-uniformity factor respectively for different SS designs. Air velocity is calculated at the mid length of the battery module in all channels. It is noticed that the air velocity is not uniform in all channels for the base design (SS-Ia). The velocity of air directly signifies the air flow distribution around the battery cells. It can be noticed from Fig. 4 (a) that the air flow rate is lowest in the 1st channel (nearest to the inlet port), and it increases gradually as moving towards the right-side wall, and the flow rate is highest in the 13th channel (nearest to the outlet port). The velocity non-uniformity factor (α) is 67% for the current base design as shown in Fig. 4 (b). The effect of non-uniform velocity distribution is also noticed on the temperature distribution of the battery cells, and it is found that T_{max} is 43.9 °C and ΔT_{max} is 8.1 °C for the battery pack. Thus, none of the conditions is satisfied for base design to obtain the optimum performance of the Li-ion battery pack.

In the present work, efforts have been made to limit temperature rise and fluctuation by following a very simplistic approach of changing the location of inlet and outlet ports. In the SS-

Ia design, the flow rate is higher for the channels near the outlet port, whereas lower flow rate is noticed for the channels nearer to the inlet port. Therefore, to mitigate this anomaly of flow non-uniformity, both inlet and outlet ports are kept on the same side for the SS-Ib design. Similar approach is also adopted by Ref. [31]. It is noticed that for the SS-Ib design, α is reduced by 56.6% as compared to the base case (SS-Ia). The location of inlet and outlet ports on the same side helped to increase the mass flow of air in the channels closer to the inlet port by restricting the flow across the far end channels. A minor rise of 1.8% in the pressure drop penalty is also observed (Table 5) which is insignificant as compared to the achieved uniformity in the flow distribution. Furthermore, the SS-II design is selected in such a manner that outlet ports are provided on both sides to remove the effect of outlet port location, while the location of inlet port is kept unchanged. Atmospheric pressure outlet boundary condition is assigned on both the outlet ports. It is noticed that α is reduced by 24.8% for the S-II design as compared to the design SS-Ia. Thus, the S-II design is not as advantageous as observed for the SS-Ib case. In the SS-Ib case, the flow through the far end channels is restricted due to the increased resistance to the fluid flow in the outlet manifold, whereas in the SS-II design, the flow from the far end channels can easily exit through the nearer outlet port (outlet port on right-side wall). Thus, no significant improvement in the flow distribution pattern is observed, and flow distribution of the SS-Ia and S-II designs are almost similar. However, a large reduction of 36.9% in the pressure drop penalty is observed for the SS-II design as given in Table 5, which highlights its potential to maintain better flow distribution characteristics at low pressure drop as compared to the SS-Ia design.

Contrary to the SS-II design, in the design SS-III, the effect of adding an additional inlet port is investigated while position of the outlet port is kept same as that of SS-Ia design. It is found that similar to the SS-II case, the SS-III design also leads to reduction of ~25% in the velocity non-

uniformity factor. However, the flow distribution pattern of the SS-III design is entirely opposite than the SS-II design. In the SS-II design, the lower flow rate is observed in the channels near left-side wall while the flow rate is higher in the channels near the right-side wall. It is observed due to the high momentum of air flow towards the right-side wall in the inlet manifold for the S-II design. After striking the side wall, the flow enters the neighboring channels, and the position of outlet port on the right-side wall further offers a low resistance path for fluid to exit, whereas for the channels near to the left-side wall, addition of an additional outlet port provides a free exit path and decreases the associated resistance in the outlet manifold. In the SS-III design, a striking effect is noticed in the inlet manifold due to positioning of the inlet ports on the opposite side walls. This impinging effect is expected to normalize the flow distribution in the inlet manifold, and its effect is also noticed on the reduction of α for the SS-III design. However, biased position of the outlet port on the right-side wall leads to non-uniformity in the flow distribution among different channels. Moreover, the biasness associated with location of the outlet port is removed in the SS-IV design by providing outlet port on both sides. It is found that for the SS-IV design, α is reduced by 84% as compared to SS-Ia design. Due to the symmetric location of both the inlet and outlet ports, the distribution of flow is also symmetric for the channels near the left and right-side walls. It can be clearly observed from velocity distribution of the SS-IV design that the flow is almost uniform in all channels. Nonetheless, cost and complexity of the cooling system increase for the SS-III and SS-IV designs due to the requirement of an additional inlet port which involves addition of either an additional fan on the second inlet port or dividing the inlet from 1^{st} fan into two symmetric pipes. On the other hand, the benefits offered by SS-II design are more alluring due to significant reduction in the pressure drop penalty as compared to the SS-III design.

4.1.2 Comparison of fluid flow distribution for SF designs

In the side inlet and front outlet (SF) designs, the location of outlet port(s) is parallel to the length of the channels and location of inlet port is on the side wall(s) as shown in Fig. 2 (b). Therefore, to understand the effect of change in the location of outlet port from side outlet to the front outlet, the results of SF-I, SF-II, SF-III and SF-IV designs are compared with the results of SS-Ia, SS-II, SS-III, and SS-IV designs, respectively. Fig. 5 (a) and (b) show velocity distribution in the different channels and α, respectively, for different SF designs. It is noticed that just by changing the location of outlet port from side outlet case (SS-Ia) to front outlet (SF-I), α is reduced by 63%. Likewise, the flow distribution uniformity is also significantly higher for other SF designs as compared to the SS designs (Fig. 4 and Fig. 5). It is noticed that $\alpha < 25\%$ for all the SF designs as shown in Fig. 5 (b). It is evaluated that α is reduced by 57.2%, 64% and 21.3% for SF-II, SF-III and SF-IV designs as compared to the SS-II, SS-III and SS-IV designs respectively. Therefore, for similar number of inlet and outlet ports, it suggested to use front outlet port location as compared to the side outlet port location. However, the pressure drop penalty also increases as the outlet port location is changed to front wall(s) as compared to the outlet port location on the side wall(s) (Table 5). It is noticed due to increase of fluid flow resistance in the outlet manifold. The issue of high pressure drop penalty is eliminated for the new proposed design with open outlet manifold, and it is noticed that the new design (SF-V) offered significantly better flow distribution uniformity as compared to SS designs (except SS-IV) at very low pressure drop. The pressure drop and α is reduced by 40.1% and 64.6%, respectively for the SF-V design as compared to the SS-Ia design which highlights the effectiveness of SF-V design to provide better fluid flow distribution at much lesser pressor drop.

Furthermore, among different SF designs, α is reduced by 12.7%, 27.1%, and 65.2% for SF-II, SF-III, and SF-IV designs, respectively, as compared to the SF-I case. It is found that similar to

the SS-IV design (with two inlet and outlet port), the best flow distribution uniformity is maintained for the SF-IV design. Yet the reduction in α is ~65% for the SF-IV design as compared to the SF-I design, whereas for the SS-IV design α is reduced by ~84% as compared to the SS-Ia design. The design with two outlet ports and one inlet port (SF-II) offered only 12.7% improvement in the flow distribution uniformity as compared to the SF-I case, whereas the improvement for the SS-II is ~25% as compared to the SS-Ia. However, reduction in pressure penalty is ~37.1% for both SS-II and SF-II designs as compared to the corresponding base designs (SS-Ia and SF-I respectively). On the other hand, for the SF-III design α is reduced by 27.1% similar to the improvement for the SS-III design as compared to the corresponding base designs. Furthermore, for the new design (SF-V), no improvement in flow distribution uniformity is noticed however, pressure drop penalty is reduced by 46% as compared to the SF-I design. Therefore, it is expected that the usefulness of the proposed new design can be best studied by maintaining same pressure drop for all designs, and it is reported in section 4.4. In the following section, temperature distribution for all the designs is compared.

4.2 Temperature distribution

4.2.1 Comparison of temperature distribution for SS designs

Li-ion battery cycle life is governed by the maximum working temperature as well as temperature difference among different battery cells; therefore, an efficient thermal management system for the battery cooling is expected to limit the temperature rise while maintaining the uniformity of temperature distribution. Temperature contours and average cell temperature distribution for different designs are compared in Fig. 6 and 7 respectively. Furthermore, in Fig. 8, T_{max} and ΔT_{max} are compared. It is noticed that among the SS designs, magnitude of T_{max} is highest for the SS-Ia design followed by SS-III and SS-II designs, whereas T_{max} is lowest for the SS-IV

design followed by SS-Ib design as shown in Fig. 8 (a). It is observed that due to high non-uniformity of velocity distribution for the SS-Ia design, the non-uniformity of temperature is also highest; as a result, formation of hotspot (high temperature zone) is observed for the cells closer to the left-side wall (Fig. 6(a) and 7(a)). The presence of an additional full channel near to the left-side walls (1st channel) facilitates in enhancing the heat dissipation from the 1st battery cell and limits its temperature rise. Furthermore, the enhanced heat transfer effect due to the additional full channel is also propagated for the second battery cell as its temperature is also lower than the 3rd battery cell (Fig. 7(a)). Similarly, the enhanced cooling effect is also noticed for the right-side channels, and the resultant lower temperature magnitude leads to lower average temperature of the battery pack. Furthermore, the temperature rise is also higher for the SS-II and SS-III designs (Fig. 8). The T_{max} and ΔT_{max} are reduced by 0.7 and 1.2 °C for the SS-II design as compared to the base design (SS-Ia). For the SS-III case, T_{max} and ΔT_{max} are reduced by 0.8 and 0.9 °C, respectively, as compared to the SS-Ia design. Moreover, pressure drop is reduced by 36.9% for the SS-II, whereas an additional fan or separate flow distribution network is needed for the SS-III design. Therefore, it can be concluded that apart from its simple and economically viable design, the SS-II case also maintained better thermo-hydraulic performance as compared to the SS-Ia and SS-III designs. Design SS-Ib leads to improvement in the air flow distribution and lowers the T_{max} and ΔT_{max} by 1.2 and 1.4 °C, respectively, as compared to the SS-Ia design. Therefore, the improvement in the thermal performance is better than the SS-II and SS-III designs. Furthermore, for the SS-IV design, effect of uniform fluid flow distribution can be clearly observed from the temperature contours as shown in Fig. 6 (e), where the hotspots are significantly mitigated. It is found that T_{max} is reduced by 2.2 °C and ΔT_{max} is reduced by 3.5 °C (43% reduction) for the SS-IV design as compared to the SS-Ia design. Nonetheless, none of the SS designs is able to meet both of the desired conditions

for the optimal thermal performance of the Li-ion battery pack (Fig. 8). Although design SS-IV is able to limit the $\Delta T_{max} < 5$ °C as shown in Fig. 8 (b), value of $T_{max} > 40$ °C makes it unfit under current boundary conditions.

4.2.2 Comparison of temperature distribution for SF designs

The SF designs offer better air flow distribution which also results in better uniformity of temperature distribution (Fig. 6 (f) – 6 (i)). It is noticed that just by changing the location of outlet port(s), ΔT_{max} is reduced by 2.4 °C, 1.8 °C, 1.7 °C and 0.4 °C for the SF-I, SF-II, SF-III and SF-IV designs as compared to the SS-Ia, SS-II, SS-III and SS-IV designs, respectively. Furthermore, ΔT_{max} is reduced by 60%, 46.6%, 49% and 19% for the SF-I, SF-II, SF-III and SF-IV designs as compared to the SS-Ia, SS-II, SS-III and SS-IV designs, respectively. The significantly higher deviation in the magnitude of V_{max} and V_{min} is responsible for high temperature non-uniformity for the SS designs (except SS-IV). The deviation in the velocity distribution is considerably lower for the SF designs which lead to reduction in the T_{max} and ΔT_{max}. Furthermore, it is noticed that $\Delta T_{max} < 5$ °C for all the SF designs which can be accredited to the better fluid flow distribution. Therefore, it can be concluded that the SF designs not only provide better fluid flow distribution for the battery pack but also maintain desired temperature difference among different battery cells. However, $T_{max} > 40$ °C for SF designs therefore, under current boundary conditions the SF designs are also not recommended for the thermal management of Li-ion battery pack. Furthermore, it is noticed that the presence of full 1st channel is advantageous in lowering the maximum temperature rise of the SS-Ia and SS-II designs as shown in Fig. 7(a). Likewise, the 13th channel is responsible for lowering temperature rise of the SS-Ib and SS-III designs. However, the presence of full channels near the side walls (1st and 13th channels) aggravates the issue of temperature non-uniformity for designs with uniform fluid flow distribution (SS-IV, SF-I, SF-II, SF-III and SF-IV

designs). Therefore, the temperature non-uniformity of these designs (SS-IV, SF-I, SF-II, SF-III and SF-IV designs) can be further curtailed by proving only a half channel near the side walls. In the following sub-section, effect of change in flow rate is studied on the thermal performance of the battery pack for different flow configurations.

4.3 Effect of inlet velocity

One of the simplest ways to control the temperature rise is increasing the inlet flow rate; however, due to the absence of any disturbance in the flow direction, its influence on the heat transfer enhancement is limited. Furthermore, increase in flow rate also comprises an additional pressure drop penalty and perhaps requires a special fan in certain cases. The change in flow rate also influences the flow distribution among different parallel channels; consequently, it alters the temperature distribution in the battery pack. In this section, the effect of change in air flow rate is studied on the velocity and temperature distribution for different designs.

Fig. 9 compares velocity non-uniformity factor for all designs at different inlet air flow rates. In general, it is found that the non-uniformity of velocity distribution increases with the increase of V_{in}, whereas temperature non-uniformity decreases with the increase of V_{in}. It is noticed that α η increases from 52% to 78% for the SS-Ia design as V_{in} is increased from 2.4 to 5.6 m/s. The increase in α is due to more momentum transfer towards the channels near to the right-side wall, and the channels closer to the left-side wall received comparatively lesser flow which amplifies the velocity distribution non-uniformity. Surprisingly, better velocity distribution uniformity is maintained by the SS-Ib design for all flow rates, and α is maintained at 30 ± 2% for different flow rates which indicates the independency of velocity distribution on the magnitude of V_{in} for the SS-Ib. On the other hand, for the designs SS-II and SS-III, analogous to the SS-Ia design, the non-uniformity in velocity distribution rises significantly with the increase of flow rate. The velocity

non-uniformity factor increases from 35.9% to 56% for SS-II and 40.5% to 57.7% for SS-III as the inlet velocity is increased from 2.4 to 5.6 m/s. Although α increases from 9.6% to 13% as the inlet velocity is increased from 2.4 to 5.6 m/s for the SS-IV design also, the uniformity in the velocity distribution is best at all inlet velocities among all SS designs. Moreover, uniformity in the air flow distribution is significantly higher for all SF designs as compared to the SS designs. Best flow distribution characteristics are noticed for SF-IV design, where α varies in the range of 5.5% to 9.2% as V_{in} is increased from 2.4 to 5.6 m/s. Better flow distribution is maintained by SF-III (α = 12.5% to 21.6%) as compared to the SF-II (α = 14.5% 26.9%) at different flow rates also. Among different SF designs, worst flow distribution results are noticed for the SF-I and SF-V designs.

Comparison of T_{max} and ΔT_{max} for different SS designs is shown in Fig. 10. It is noticed that for the SS-Ia design, T_{max} < 40 °C at highest studied flow rate (V_{in} 5.6 m/s); however, ΔT_{max} > 5 °C for the entire studied flow rate range. Therefore, SS-Ia design is unable to provide the desired temperature uniformity for the cooling of Li-ion battery at the studied range of flow rate. Although shoot up of T_{max} is restricted with increase of flow rate, uniformity in the temperature distribution could not be maintained due to rise of α with increase of flow rate. Similar issue is also noticed for the SS-II and SS-III designs where desired temperature uniformity is not obtained due to significant rise of α with increase of flow rate. For the SS-Ib design, ΔT_{max} < 40 °C for $V_{in} \geq 4.8$ m/s and ΔT_{max} is < 5 °C for V_{in} = 5.6 m/s; thus, SS-Ib design can be considered for EV cooling at $V_{in} \geq 5.6$ m/s. The independency of α from the V_{in} also makes SS-Ib design more suitable to be installed at higher flow rates for the effectual cooling of Li-ion battery pack. Furthermore, it is noticed that the desired T_{max} and ΔT_{max} are maintained by SS-IV at $V_{in} \geq 4.8$ m/s; therefore, $V_{in} \geq$ 4.8 m/s is found to be the preferred V_{in} range to maintain optimum operating conditions for the Li-

ion battery. Thus, among the different SS designs, only SS-Ib design for $V_{in} \geq 5.6$ m/s and SS-IV for $V_{in} \geq 4.8$ m/s can be considered to meet the desired thermal characteristics of the Li-ion battery pack.

Moreover, the perks of better flow distribution in the SF designs can be clearly observed from the T_{max} and ΔT_{max} profiles as shown in Fig. 11. It is noticed that $T_{max} < 40$ °C for all SF designs at $V_{in} \geq 4.8$ m/s, and $\Delta T_{max} < 5$ °C for all SF designs at $V_{in} \geq 4$ m/s. Therefore, $V_{in} \geq 4.8$ m/s can be considered as a desired range for maintaining the favorable conditions of the T_{max} and ΔT_{max} to insure an optimum performance of the Li-ion battery pack for all the SF designs. Furthermore, the designs: SF-II and SF-V, are found to be more alluring due to significantly lower pressure drop penalty as compared to other SF designs. Therefore, in the following subsection, the performances of various designs are compared by keeping an almost same pressure drop penalty.

4.4 Comparison at same pressure drop

The magnitude of pressure drop penalty controls the associated fluid flow rate, which significantly influences the thermal performance of different designs. The performance of all the designs is compared at pressure drop penalty of ~32 Pa as occurred for the base case (SS-Ia) at V_{in} = 4 m/s as given in Table 5. As discussed earlier also, at this condition the desired favorable conditions are not maintained by the SS-Ia design. The same is expected for the SS-Ib design also as it is unable to maintain the desired characteristics even at slightly higher pressure drop. Furthermore, it is noticed that although the velocity distribution non-uniformity is mitigated for the SS-IV design, the desired thermal characteristics are not met due to the lower overall flow rate because of higher associated pressure drop. The higher pressure drop in the SS-IV design is due to integration of two inlet ports on the opposite side walls, which lead to jet impingement effect in the inlet manifold. Therefore, SS-IV design requires higher peristaltic power to achieve the desired

temperature characteristics. Similarly, due to poor thermal performance and higher pressure drop per inlet port for the SS-III design as compared to the SS-IV (Table 5), the desired results are not expected. Therefore, among the SS designs, only the results are compared for SS-II design at pressure drop of ~32 Pa. The designs SS-II is selected due to its potential to maintain lower pressure drop at same flow rate as compared to the base case. Similarly, due to the higher pressure drop (Table 5) and unsuitability of the SF-I, SF-III and SF-IV designs to meet the desired condition, their results are also not compared and only the results of the SF-II and SF-V are compared in this section.

In Table 6, the results of base case (SS-Ia) are compared with the SS-II, SF-II, and SF-V. It is noticed that for the SS-II design, the first condition of $T_{max} < 40$ °C is maintained however, the $\Delta T_{max} > 5$ °C which limit its usability as an effectual cooling module configuration for the Li-ion battery pack. The higher temperature non-uniformity in the SS-II design is noticed due to presence of significant flow distribution non-uniformity. This problem is substantially reduced for the similar SF design (SF-II), and it can be observed that SF-II design successfully limits the rise of T_{max} and ΔT_{max} under the desired limits. Furthermore, the best results are noticed for the new proposed design (SF-V). It is noticed that T_{max} is reduced by 7 °C and fluctuation in temperature distribution is reduced by 65% by the SF-V design as compared to the base design (SS-Ia) at same pressure drop. Thus, SF-V design is best suited for the effectual air-cooling of Li-ion battery pack in maintaining best thermal performance at minimal pressured drop penalty.

Nonetheless, SF-V design cannot be recommended for liquid cooling operations due to its inability to provide necessarily outlet port for the liquid collection. The liquid cooling or two-phase cooling is required for the heavy-duty applications where the air-cooling modules are inadequate to maintain the desired rates of heat dissipation. Therefore, SF-II design is suggested to be used in

liquid cooling / phase change cooling modules. Furthermore, it will be exciting to the applicability of current proposed design at variable battery discharge rates under unsteady rates of heat generation.

4.5 Effect of variable air thermophysical properties

Finally, the effect of variable air thermophysical is studied on the thermal and hydrodynamic performance of air-cooling module of SS-Ia design. SS-Ia design is considered for the comparison due to the occurrence of maximum temperature rise, which is expected to have the highest effect on air thermophysical properties. In Fig. 12, the velocity and temperature distribution results are compared for the cases with constant and variable thermophysical properties. It is noticed that the pattern of velocity distribution remains the same for both the cases (Fig. 12 (a)) because no heat is supplied in the inlet manifold. Whereas a slight rise in the velocity magnitude is noticed in all channels due to decrease in the density and viscosity of the air with temperature rise along the flow direction. Furthermore, it is found that the effect of variable air thermophysical properties is insignificant on the temperature distribution in the battery pack and the maximum temperature deviation is < 0.15 °C (Fig. 12 (b)). Therefore, it can be concluded that assuming the constant thermophysical properties of air in the current work are sufficient to predict the thermal and hydrodynamic performance of the battery cooling modules.

5. CONCLUSION

In the current work, effect of two common air flow configurations: side inlet and side outlet (SS) and side inlet and front outlet (SF), with different number of inlet/ outlet ports (single inlet and single outlet, single inlet and two outlets, two inlets and single outlet, and two inlets and two outlets) has been studied for thermal management of Li-ion battery pack with 12 prismatic cells.

Subsequently, a new design of battery module with best thermal and hydrodynamic performance is proposed. Followings are major conclusion from the current numerical work:

1. It is noticed that the best flow distribution uniformity is provided by the design with two inlet and two outlet ports for both the SS and SF configurations. However, addition of two inlet ports increases the pressure drop and complexity of cooling module.
2. The location of outlet port significantly influences the distribution of fluid in the channels, and the uniformity in the flow distribution is significantly higher for the SF designs as compared to the SS designs.
3. It is more beneficial to add two outlet ports (SS-II design) as compared to the configurations of two inlet ports (SS-III design) for the SS case. Whereas, for the SF designs, addition of two inlet ports is found to be more advantageous as compared to addition of two outlet ports (SF-II).
4. Non-uniformity in the velocity distribution increases with increase of flow rate except for SS-Ib design where the SS-Ib design maintained almost consistent fluid flow distribution trend for the studied range of flow rate.
5. Among all SS designs, only SS-Ib at $V_{in} \geq 5.6$ m/s and SS-IV at $V_{in} \geq 4.8$ m/s are found suitable for the thermal management of Li-ion battery pack at the studied range of flow rate. Whereas all SF designs maintained desired T_{max} and ΔT_{max} conditions at $V_{in} \geq 4.8$ m/s.
6. At same pressure drop, the best T_{max} and ΔT_{max} conditions are maintained by new proposed design (SF-V). The new design results in reduction of T_{max} by 7 °C and ΔT_{max} by 64.5% as compared to base design (SS-Ia) at same pressure drop penalty; therefore, SF-V design is recommended as air-cooling modules for the effective thermal management of Li-ion battery packs.

NOMENCLATURE

AD	absolute deviation
c_p	specific heat (J/kg/K)
EV	electric vehicle
H	height
L	length
N	number
Nu	Nusselt number
P	pressure (Pa)
Re	Reynolds number
T	temperature (°C)
V	velocity (m/s)
W	width

Greek symbols

α	velocity non-uniformity factor
μ	dynamic viscosity (Pa s)
ρ	density (kg/m^3)
λ	thermal conductivity (W/m/K)

Subscript

a	air
avg	average
ch	channel

in	inlet
max	maximum
min	minimum
s	solid

REFERENCES

1. United Nations Climate Change, The Paris Agreement, https://unfccc.int/process-and-meetings/the-paris-agreement/the-paris-agreement (accessed February 04, 2022).
2. Lin, B., Xu, B., 2018 "How to promote the growth of new energy industry at different stages?" Energy Policy, 118, pp. 390–403.
3. Yu, H., Fan, J.L., Wang, Y., Wang, J., 2018, "Research on the new-generation urban energy system in China," Energy Procedia, 152, pp. 698–780.
4. Yang, D., Qiu, L.S., Yan, J.J., Chen, Z., 2019 "The government regulation and market behavior of the new energy automotive industry," J. Clean. Prod., 210, pp. 1281–1288.
5. Thakur, A.K., Prabakaran, R., Elkadeem, M.R., Sharshir, S.W., Arıcı, M., Wang, C., Zhao, W., Hwang, J.Y., Saidur, R., 2020, "A state of art review and future viewpoint on advance cooling techniques for Lithium–ion battery system of electric vehicles," J. Energy Storage, 32, p. 101771.
6. Lu, M., Zhang, X., Ji, J., Xu, X., Zhang, Y., 2020, "Research progress on power battery cooling technology for electric vehicles," J. Energy Storage, 27, p. 101155
7. Zichen, W., Changqing, D., 2021, "A comprehensive review on thermal management systems for power lithium-ion batteries," Renew. Sustain. Energy Rev., 139, p. 110685.
8. Wang, X., Li, B., Gerada, D., Huang, K., Stone, I., Worrall, S., Yan, Y., 2022, "A critical review on thermal management technologies for motors in electric cars," Appl. Therm. Eng., 201, p. 117758.
9. IEA, 2017 "IEA Technology collaboration programme on energy efficient end-user equipment (4E)," https://www.iea-4e.org/.

10. Fan, Y., Bao, Y., Ling, C., Chu, Y., Tan, X., Yang, S. 2019, “Experimental study on the thermal management performance of air cooling for high energy density cylindrical lithium-ion batteries,” Appl. Therm. Eng., 155, pp. 96–109.

11. Karimi, G., Dehghan, A., 2014, “Thermal analysis of high-power lithium-ion battery packs using flow network approach,” Int. J. Energy Res., 38, pp. 1793–1811.

12. Beheshti, A., Shanbedi, M., Heris, S.Z., 2014, “Heat transfer and rheological properties of transformer oil-oxidized MWCNT nanofluid,” J. Therm. Anal. Calorim., 118, pp. 1451–1460.

13. Huo, Y., Rao, Z., 2015, “The numerical investigation of nanofluid based cylinder battery thermal management using lattice Boltzmann method,” Int. J. Heat Mass Transfer, 91, pp. 374–384.

14. Selvam, C., Lal, D.M., Harish, S., 2016, “Thermal conductivity enhancement of ethylene glycol and water with graphene nanoplatelets,” Thermochim. Acta, 642, pp. 32–38.

15. Sidney, S., Dhasan, M.L., Harish, S., 2019, “Experimental investigation of freezing and melting characteristics of graphene-based phase change nanocomposite for cold thermal energy storage applications,” Appl. Sci., 9 (6), p. 1099.

16. Jilte, R., Kumar, R., Ahmadi, M.H., 2019 “Cooling performance of nanofluid submerged vs. nanofluid circulated battery thermal management systems,” J. Cleaner Prod., 240, p. 118131.

17. Wang, S., Lin, Z., Zhang, W., Chen, J., 2009, “Experimental study on pulsating heat pipe with functional thermal fluids,” Int. J. Heat Mass Transfer, 52, pp. 5276–5279.

18. Burban, G., Ayel, V., Alexandre, A., Lagonotte, P., Bertin, Y., Romestant, C., 2013, "Experimental investigation of a pulsating heat pipe for hybrid vehicle applications," Appl. Therm. Eng., 50, pp. 94–103.

19. Rao, Z., Huo, Y., Liu, X., 2014, "Experimental study of an OHP-cooled thermal management system for electric vehicle power battery," Exp. Therm. Fluid Sci., 57, pp. 20–26.

20. Ye, Y., Saw, L.H., Shi, Y., Tay, A.A., 2015, "Numerical analyses on optimizing a heat pipe thermal management system for lithium-ion batteries during fast charging," Appl. Therm. Eng., 86, pp. 281–291.

21. Rao, Z., Huo, Y., Liu, X., Zhang, G., 2015, "Experimental investigation of battery thermal management system for electric vehicle based on paraffin/copper foam," J. Energy Inst., 88 (3), pp. 241–246.

22. Wang, Z., Zhang, Z., Jia, L., Yang, L., 2015, "Paraffin and paraffin/aluminum foam composite phase change material heat storage experimental study based on thermal management of Li-ion battery," Appl. Therm. Eng., 78, pp. 428–36.

23. Jiang, G., Huang, J., Fu, Y., Cao, M., Liu, M., 2016, "Thermal optimization of composite phase change material/expanded graphite for Li-ion battery thermal management," Appl. Therm. Eng., 108, pp. 1119–1125.

24. Ping, P., Peng, R., Kong, D., Chen, G., Wen, J., 2018, "Investigation on thermal management performance of PCM-fin structure for Li-ion battery module in high-temperature environment," Energy Convers. Manag., 176, pp. 131–146.

25. Zhang, J., Shao, D., Jiang, L., Zhang, G., Wu, H., Day, R., Jiang, W., 2022, "Advanced thermal management system driven by phase change materials for power lithium-ion batteries: A review, Renew. Sust., Energy Rev., (accepted on 28 Jan 2022).

26. Qin, P., Liao, M., Zhang, D., Liu, Y., Sun, J., Wang, Q., 2019, "Experimental and numerical study on a novel hybrid battery thermal management system integrated forced-air convection and phase change material," Energy Convers. Manag., 195, pp. 1371-1381.

27. Mahamud, R., Park, C., 2011, "Reciprocating air flow for Li-ion battery thermal management to improve temperature uniformity," J. Power Sources, 196, pp. 5685–5696.

28. Na, X., Kang, H., Wang, T., Wang, Y., 2018, "Reverse layered air flow for Li-ion battery thermal management," Appl. Therm. Eng., 143, pp. 257–262.

29. Shahid, S., Agelin-Chaab, M., 2018, "Development and analysis of a technique to improve air-cooling and temperature uniformity in a battery pack for cylindrical batteries," Therm. Sci. Eng. Prog., 5, pp. 351–363.

30. E, J., E, Yue, M., Chen, J., Zhu, H., Deng, Y., Zhu, Y., Zhang, F., Wen, M., Zhang, B., Kang, S., 2018, "Effects of the different air cooling strategies on cooling performance of a lithium-ion battery module with baffle," Appl. Therm. Eng., 144, pp. 231–241.

31. Wang, Y.W., Jiang, J.M., Chung, Y.H., Chen, W.C., Shu, C.M., 2019, Forced-air cooling system for large-scale lithium-ion battery modules during charge and discharge processes, J. Therm. Anal. Calorim., 135, pp. 2891-2901.

32. Fan, L., Khodadadi, J.M., Pesaran, A.A., 2013, "A parametric study on thermal management of an air-cooled lithium-ion battery module for plug-in hybrid electric vehicles," J. Power Sources, 238, pp. 301-312.

33. Xie, J., Ge, Z., Zang, M., Wang, S., 2017, “Structural optimization of lithium-ion battery pack with forced air cooling system,” Appl. Therm. Eng., 126, pp. 583–593.

34. Hong, S., Zhang, X., Chen, K., Wang, S., 2018, “Design of flow configuration for parallel air-cooled battery thermal management system with secondary vent,” Int. J. Heat Mass Transfer, 116, pp. 1204–1212.

35. Chen, K., Wang, S., Song, M., Chen, L., 2017, “Structure optimization of parallel air-cooled battery thermal management system,” Int. J. Heat Mass Transfer, 111, pp. 943–952.

36. Liu, Z., Wang, Y., Zhang, J., Liu, Z., 2014, “Shortcut computation for the thermal management of a large air-cooled battery pack,” Appl. Therm. Eng., 66, pp. 445-452.

37. Chen, K., Song, M., Wei, W., Wang, S., 2019, “Design of the structure of battery pack in parallel air-cooled battery thermal management system for cooling efficiency improvement,” Int. J. Heat Mass Transfer, 132, pp. 309–321.

38. Li, X., He, F., Zhang, G., Huang, Q., Zhou, D., 2019, “Experiment and simulation for pouch battery with silica cooling plates and copper mesh based air cooling thermal management system,” Appl. Therm. Eng., 146, pp. 866–880.

39. Wang, S., Li, K., Tian, Y., Wang, J., Wu, Y., Ji, S., 2019, “Improved thermal performance of a large laminated lithium-ion power battery by reciprocating air flow,” Appl. Therm. Eng., 152, pp. 445–454.

40. Liu, Y., Zhang, J., 2019, “Design a J-type air-based battery thermal management system through surrogate-based optimization,” Appl. Energy, 252, p. 113426.

41. Kang, D., Lee, P.-Y., Yoo, K., Kim, J., 2020, “Internal thermal network model-based inner temperature distribution of high-power lithium-ion battery packs with different shapes for thermal management,” J. Energy Storage, 27, p. 101017.

42. Zhang, F., Lin, A., Wang, P., Liu, P., 2022, “Optimization design of a parallel air-cooled battery thermal management system with spoilers,” Appl. Therm. Eng., 182, P. 116062.

43. Ma, R., Ren, Y., Wu, Z., Xie, S., Chen, K., Wu, W., 2022, “Optimization of an air cooled battery module with novel cooling channels based on silica cooling plates,” Appl. Therm. Eng., 213, p. 118650.

44. Nacke, R., Northcutt, B., Mudawar I., 2011, “Theory and experimental validation of cross-flow micro-channel heat exchanger module with reference to high Mach aircraft gas turbine engines,” Int. J. Heat Mass Transfer, 54, pp. 1224–1235.

45. Kumar, R., Singh, G., Mikielewicz, D., 2018, “A New Approach for the Mitigating of Flow Maldistribution in Parallel Microchannel Heat Sink,” J. Heat Transfer, 140 (7), p. 072401.

46. Kumar, R., Singh, G., Mikielewicz, D., 2019 “Numerical Study on Mitigation of Flow Maldistribution in Parallel Microchannel Heat Sink: Channels Variable Width Versus Variable Height Approach,” J. Electron. Packag., 141 (2), p. 021009.

List of Tables

List of Figures

Fig. 7 Comparison of average temperature distribution for (a) SS and (b) SF designs at V_{in} = 4 m/s

Fig. 8 Comparison of (a) T_{max} and (b) ΔT_{max} for SS and SF designs at V_{in} = 4 m/s

Fig. 9 Comparison of velocity non-uniformity factor for (a) SS and (b) SF designs at different V_{in}

Fig. 10 Comparison of (a) T_{max} and (b) ΔT_{max} for SS designs at different V_{in}

Fig. 11 Comparison of (a) T_{max} and (b) ΔT_{max} for SF designs at different V_{in}

Fig. 12 Effect of variable thermophysical properties of air on the (a) velocity distribution and (b) temperature distribution for SS-Ia design

Table 1 Various studies on the air-cooled Li-ion battery packs

Author	Battery description	Cell capacity	Dimensions (mm)	C rate	Modification	$T_{max}/\Delta T_{max}$ (Best case)	ΔP
Cylindrical battery cells							
Mahamud and Park [27]	Cylindrical N = 8	3.6 mAh	D = 42.4 L = 97.7	7C	Reciprocating flow	T_{max} < 30 °C ΔT_{max} = 1.5 °C	-
Na et al. [28]	Cylindrical N = 20	-	D = 38 L = 120	3C	Cell capacity and rectifier	T_{max} = 38.2 °C ΔT_{max} = 4.8 °C	126 Pa
Shahid and Agelin-Chaab [29]	Cylindrical N = 32		D = 18 mm L = 65 mm	1 and 2C	Secondary inlet plenums	T_{max} < 40 °C ΔT_{max} > 5 °C	-
E et al. [30]	Cylindrical N = 60	2.6 mAh	-	0.5 and 1 C	Inlet/outlet port location and addition of baffles	T_{max} = 38.9 °C ΔT_{max} = 7.3 °C	-
Wang et al. [31]	Cylindrical N = 32	2.9 mAh	D = 18 mm L = 65 mm	1, 1.5 and 2C	Inlet/outlet port location	T_{max} > 40 °C ΔT_{max} > 5 °C	-
Prismatic / pouch type battery cells							
Xie et al. [33]	Prismatic N = 10	-	W = 16 L = 131 H = 65	-	Cell spacing, inlet/outlet plenums size and angles	T_{max} < 40 °C ΔT_{max} < 5 °C	-
Hong et al. [34]	Prismatic N = 12	2.2 mAh	W = 16 L = 155 H = 65	5 C	Secondary vent positions	T_{max} = 37.5 °C ΔT_{max} = 3.3 °C	34.8 Pa
Chen et al. [35]	Prismatic N = 8	11 W (dummy)	W = 20 L = 90 H = 16	5C	Cell spacing	T_{max} = 61 °C ΔT_{max} = 3 °C	58.1 Pa
Chen et al. [37]	Prismatic N = 12	2.2 mAh	W = 16 L = 155 H = 65	5C	Inlet/outlet plenums size and angles	T_{max} = 40.3 °C ΔT_{max} = 2.8 °C	48.6 Pa
Li et al. [38]	Pouch type N = 1, 5	16 Ah	W = 75 L = 165 H = 10	5C	Silica cooling plates and fan location	T_{max} = 45.6 °C	-
Wang et al [39]	Pouch type N = 1	37 Ah	W = 7.1 L = 268 H = 211	3 C	Reciprocating flow	T_{max} = 42.9 °C ΔT_{max} < 5 °C	-
Liu and Zhang [40]	Pouch type N = 10	-	W = 16 L = 155 H = 65	3 C	Inlet/outlet port locations and size	T_{max} < 30 °C ΔT_{max} < 2 °C	391 Pa
Zhang et al. [42]	Prismatic N = 8	-	W = 27 L = 90 H = 70	-	Addition of spoilers	T_{max} = 47.6 °C ΔT_{max} = 0.5 °C	32.5 Pa
Ma et al. [43]	Prismatic N = 8	12 Ah	W = 27 L = 90 H = 70		Silica cooling plates and tapering of inlet manifold	T_{max} = 48.9 °C ΔT_{max} = 1.9 °C	-

Table 2 Properties of Li-ion battery and air

Property	Battery	Air
Specific heat (J/kg/K)	900	1005
Thermal conductivity	240	0.0267
Density (kg/m^3)	2700	1.165
Dynamic viscousity (Pa s)	-	1.86×10^{-5}

Table 3 Air inlet parameters

V_{in} (m/s)	Flow rate (m^3/s)	Re_{in}
2.4	0.007	4598
3.2	0.009	6131
4	0.011	7664
4.8	0.013	9196
5.6	0.016	10729

Table 4 Grid independence test

No. of grid elements	T_{max} (°C)	AD (T_{max}) (%)	ΔP (Pa)	AD (ΔP) (%)
4.0×10^5	44.56	-	35.2	-
8.0×10^5	44.92	0.81	34.4	2.14
14×10^5	44.71	0.46	33.2	3.59
20×10^5	44.14	1.27	32.5	2.24
26×10^5	43.87	0.62	32.2	0.84
32×10^5	43.57	0.68	32.2	0.16

Table 5 Pressure drop for SS and SF design at V_{in} = 4 m/s

S. no.	SS Design	ΔP (Pa)	SF Design	ΔP (Pa)
1	SS-Ia	32.2	SF-I	35.3
2	SS-Ib	32.8	SF-II	22.2
3	SS-II	20.3	SF-III	37.4/inlet
4	SS-III	33.6/inlet	SF-IV	23.7/inlet
5	SS-IV	22.8/inlet	SF-V	19

Table 6 Comparison of thermal performance at similar pressure drop

Design	ΔP(Pa)	T_{max} (°C)	ΔT_{max} (°C)
SS-Ia	32.2	43.9	8.1
SS-II	32.1	39	5.3
SF-II	32.2	38.4	2.9
SF-V	32	36.9	2.8

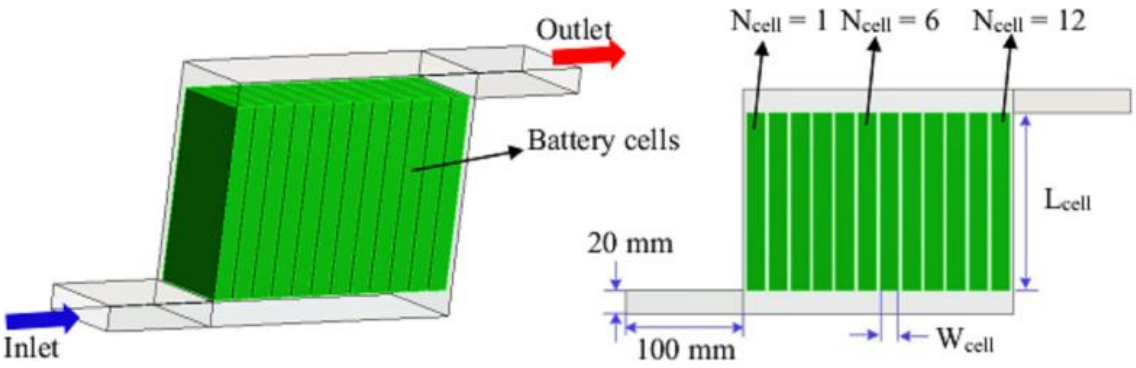

Fig. 1 Schematic 3D view of Li-ion battery pack for SS-I flow configuration

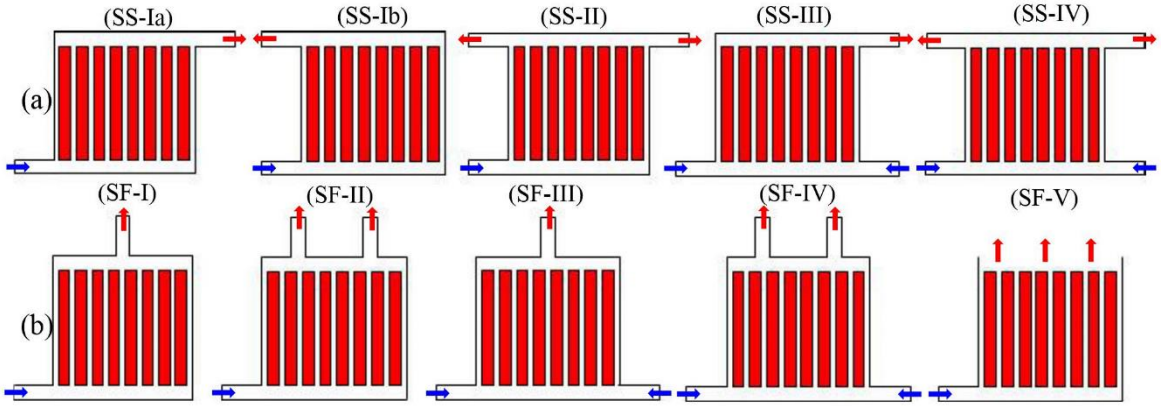

Fig. 2 Schematic of different inlet and out flow configurations: (a) side inlet and side outlet, and (b) side inlet and front outlet designs

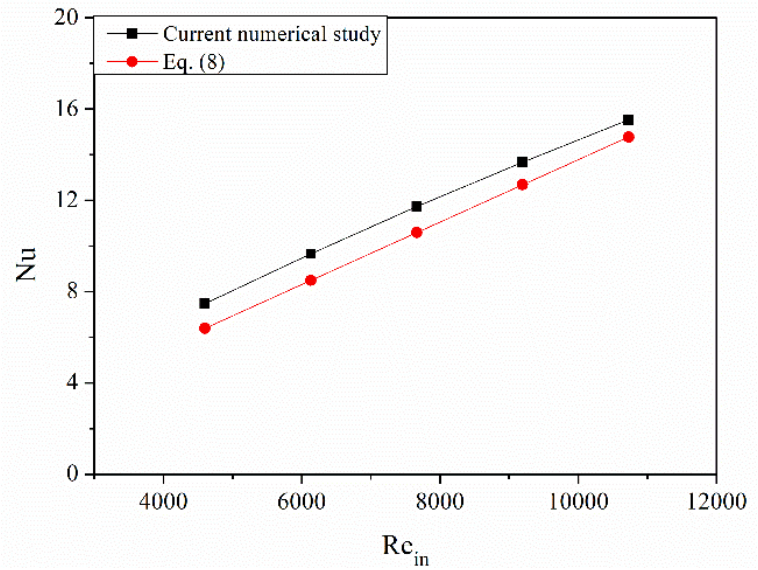

Fig. 3 Comparison of Nu for current numerical study and correlation of Nacke et al. [44]

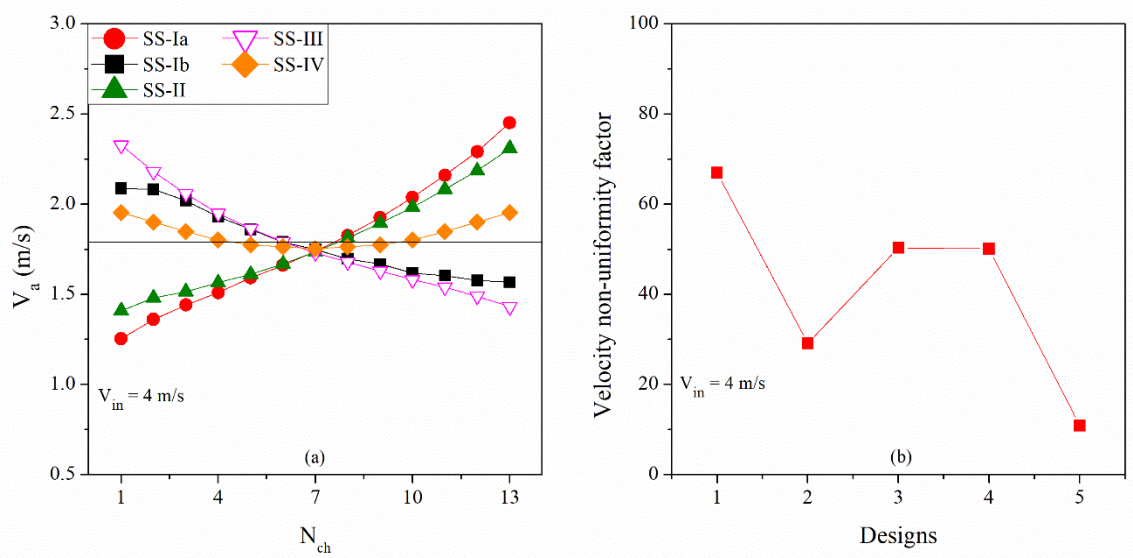

Fig. 4 Comparison of air flow distribution in the different SS designs: (a) velocity distribution and (b) velocity non-uniformity factor at V_{in} = 4 m/s

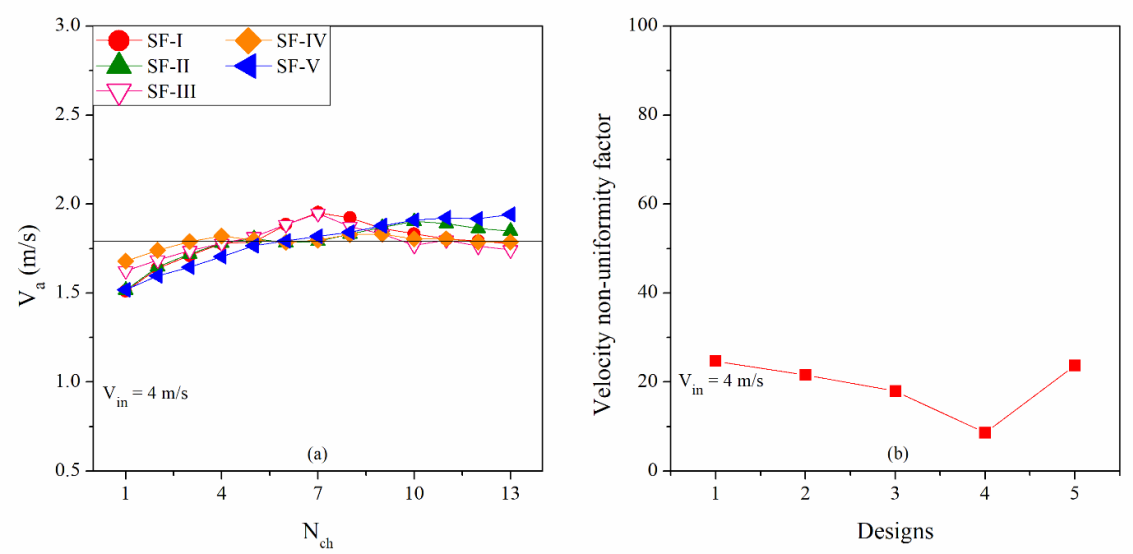

Fig. 5 Comparison of air flow distribution in the different SF designs: (a) velocity distribution and (b) velocity non-uniformity factor at V_{in} = 4 m/s

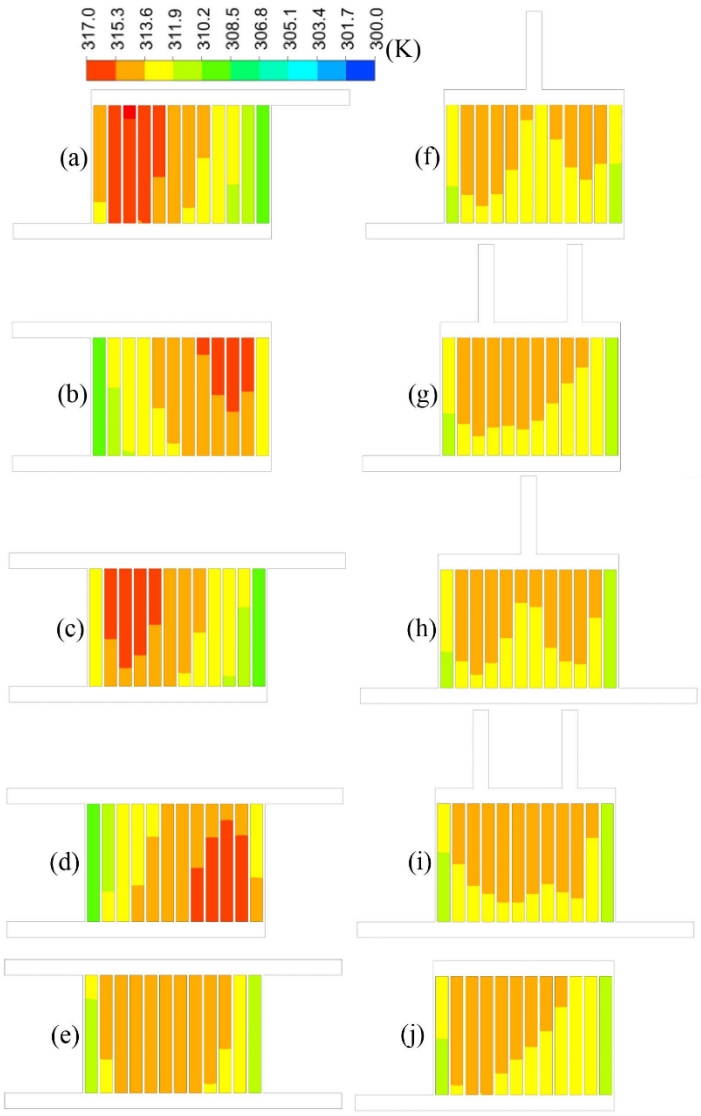

Fig. 6 Comparison of temperature contours for SS designs: (a) SS-Ia, (b) SS-Ib, (c) SS-II, (d) SS-III, (e) SS-IV and SF designs: (f) SF-I, (g) SF-II, (h) SF-III (i) SF-IV and (j) SF-V at $V_{in} = 4$ m/s

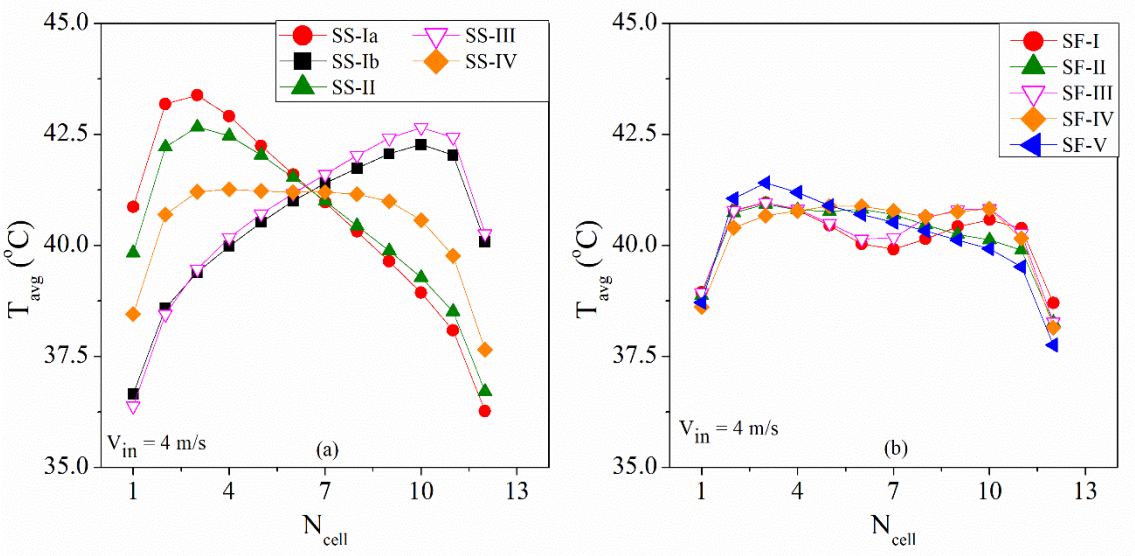

Fig. 7 Comparison of average temperature distribution for (a) SS and (b) SF designs at V_{in} = 4 m/s

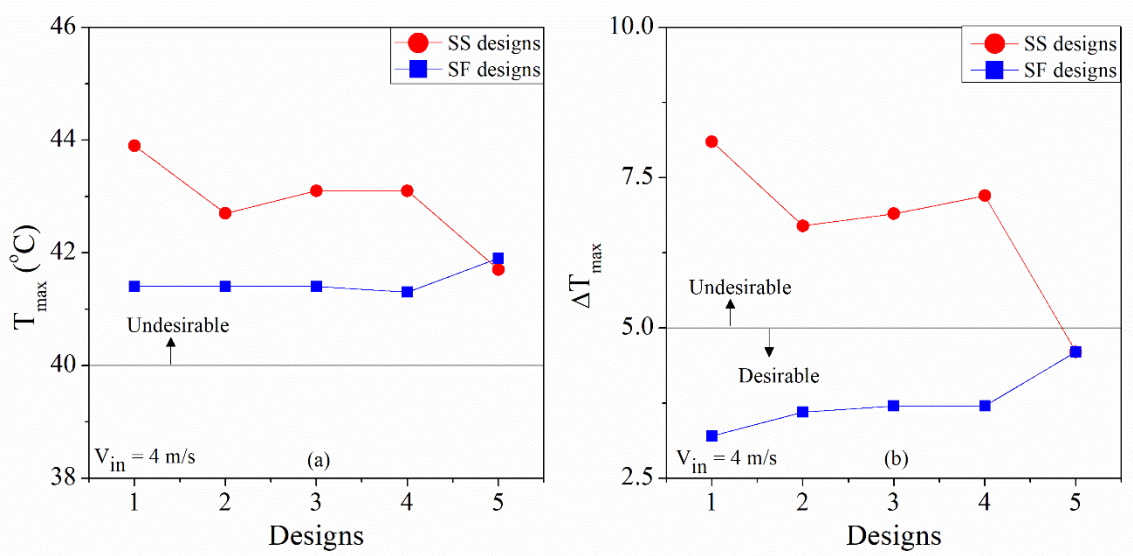

Fig. 8 Comparison of (a) T_{max} and (b) ΔT_{max} for SS and SF designs at $V_{in} = 4$ m/s

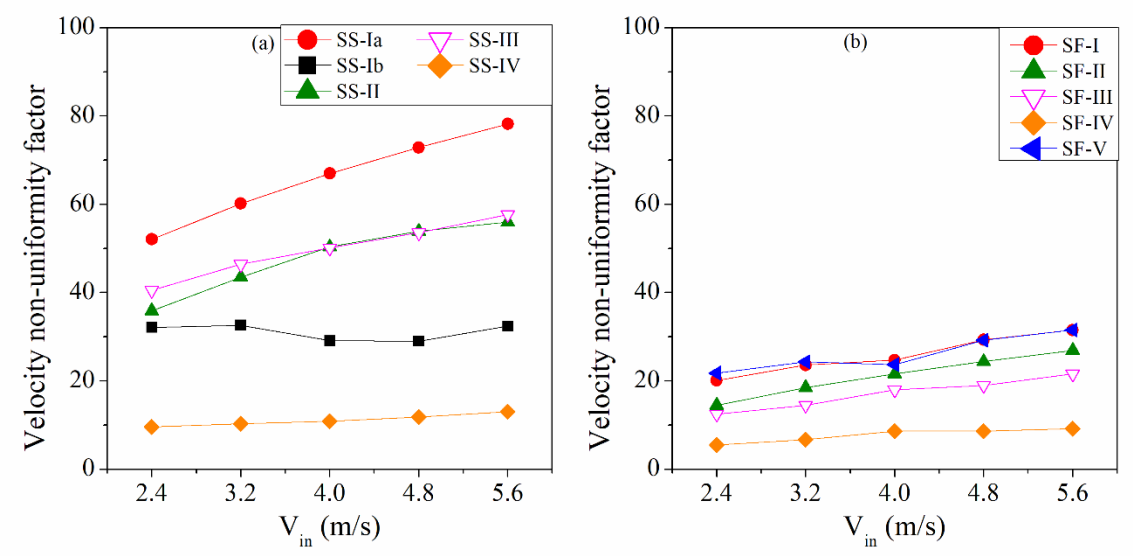

Fig. 9 Comparison of velocity non-uniformity factor for (a) SS and (b) SF designs at different V_{in}

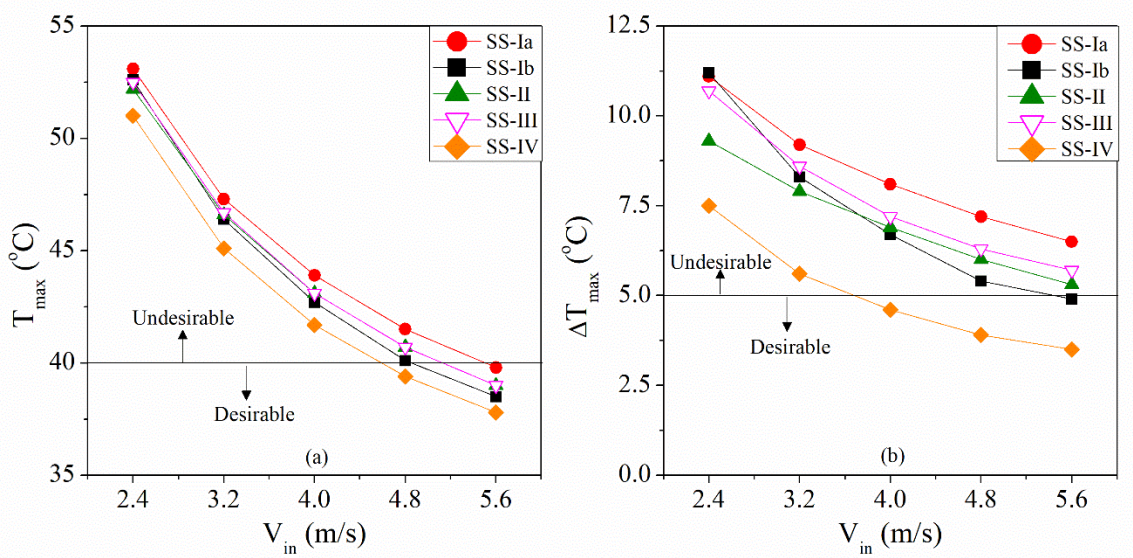

Fig. 10 Comparison of (a) T_{max} and (b) ΔT_{max} for SS designs at different V_{in}

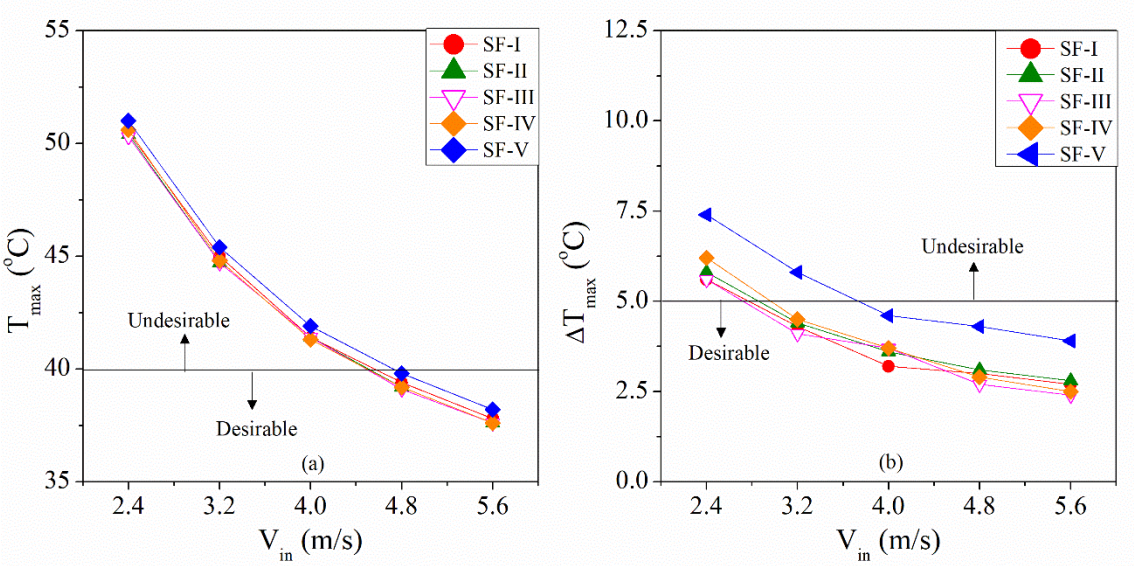

Fig. 11 Comparison of (a) T_{max} and (b) ΔT_{max} for SF designs at different V_{in}

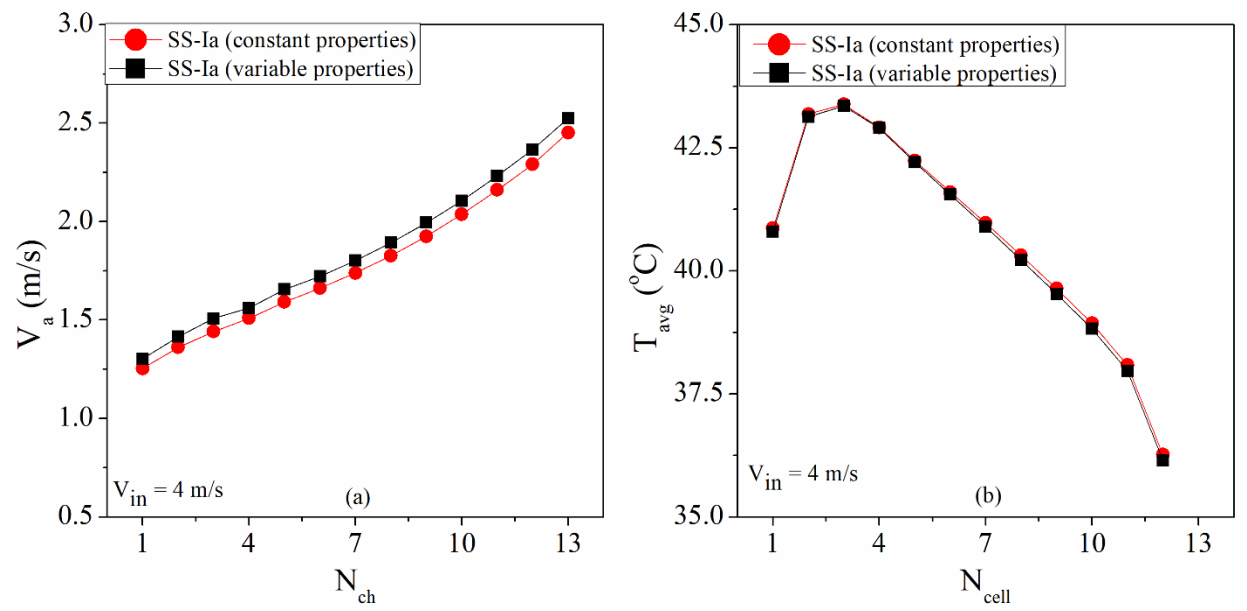

Fig. 12 Effect of variable thermophysical properties of air on the (a) velocity distribution and (b) temperature distribution for SS-Ia design